Chapter 3

Coexistence of Tetragonal and Cubic Phase Induced Complex Magnetic Behaviour in $CoMn_2O_4$ Nanoparticles

3.1 Introduction

In this chapter, we have examined the structure, microstructure and magnetic properties of $CoMn_2O_4$ nanoparticles synthesized by a facile co-precipitation method. The structure and microstructure analysis is discussed in section 3.2, show the coexistence of tetragonal (space group $I41/amd$) and cubic (space group $Fd\bar{3}m$) phase in contrast to earlier reported pure tetragonal phase (space group $I41/amd$). Although, Mn and Co occupy both octahedral and tetrahedral sites depending on valencies, Mn^{3+} and Co^{2+} dominatingly occupy B and A site, respectively. Microstructural analysis shows the semispherical shape with 95 nm size particles of $CoMn_2O_4$. The unusual magnetic properties such as two transition temperatures (Tc_1 and Tc_2), coercivity (Hc), exchange bias and vertical magnetization shift (VMS) observed from the zero field cooled (ZFC) and field cooled (FC) temperature and field dependent magnetization measurements, are discussed in section 3.3. Structure dependent magnetic properties are elaborated in section 3.4. In section 3.5, we have summarized the important findings of this chapter.

3.2 Structure and microstructure

3.2.1 Thermal Analysis through TGA

Figure 3.1 depicts the TGA and DTG curve of the raw $CoMn_2O_4$ nanoparticles. From 25 ºC to 120 ºC, weight loss is 7% which is due to the removal of absorbed water [149,150], 5% weight loss from 120 to 500 ºC is due to the removal of chloride, nitrates and hydroxides [150,151]. Beyond 500 ºC, there is a negligible weight loss in the sample. On the basis of TGA-DTG data, we have chosen the calcination temperature as 600 ºC.

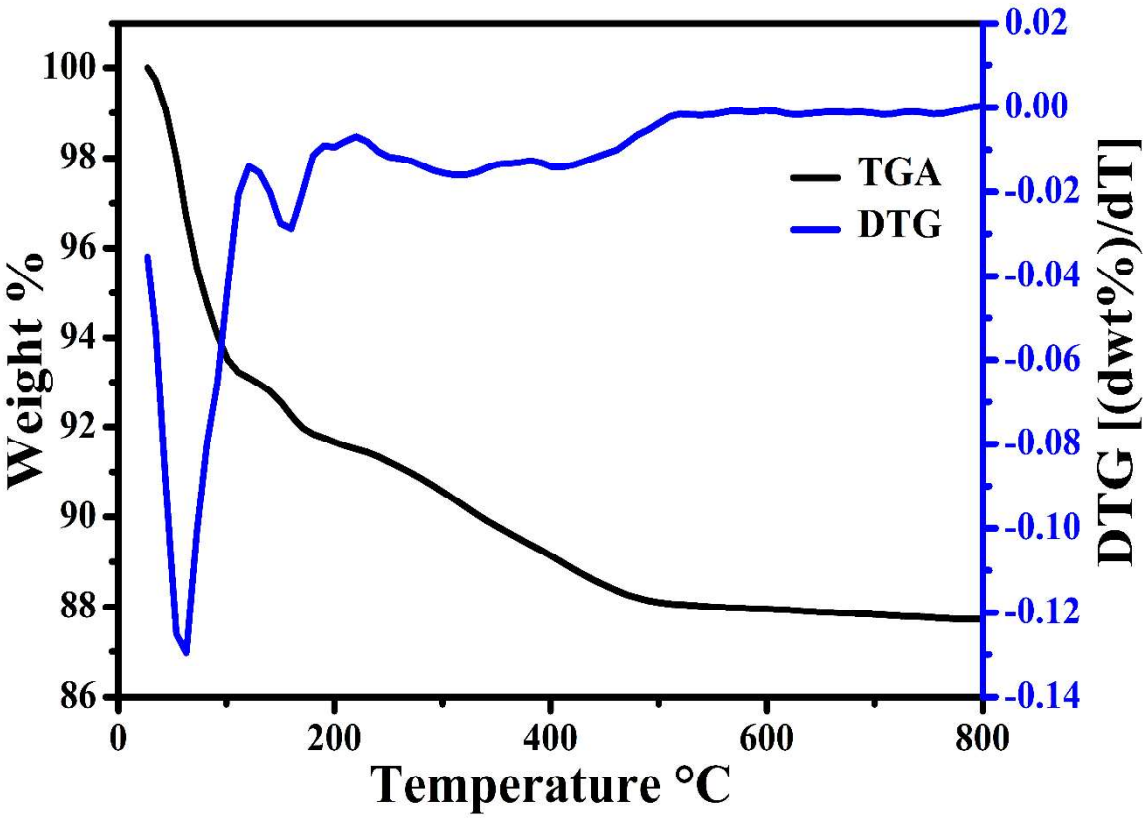

Figure 3.1: TGA and DTG of $CoMn_2O_4$ nanoparticles.

3.2.2 X-ray diffraction Analysis for Structure

X-ray diffraction depicted in **Figure 3.2**, shows the sharp peaks indicating the crystalline nature of the particles, and are well matched with the tetragonal phase, JCPDS card no. 77-0471. Few additional peaks that are present in the sample do not match with the tetragonal phase. In order to find out the phase corresponding to additional peaks, we have carried out the Rietveld refinement using FullProf software choosing pseudo-voigt as a peak profile function. The experimental, calculated, and their difference patterns are denoted as dot, solid line, and continuous bottom line, respectively **(Figure 3.2)**. The position of Bragg reflections represented by the tick marks above the difference pattern indicate the reflection planes of the tetragonal (upper tick marks) and cubic phase (lower tick marks). We observe that along with tetragonal phase, space group $I41/amd$, a cubic phase with the space group $Fd\bar{3}m$ is present. The structural parameters determined from the Rietveld refinement are listed in **Table 3.1**. The setting 2 is adopted for the unit cell origin which is fixed at the centre of symmetry, 3m in the cubic phase and 2/m in the tetragonal phase. During Rietveld refinement, cell parameters, FWHM, shape, asymmetry and thermal parameters have been refined. In the present case, the tetrahedral and octahedral position coordinates (X, Y, Z), corresponding to Co and Mn are fixed, while for oxygen, co-ordinates have been refined. The cation distribution has been chosen according to octahedral site preference energy (OSPE) value and reported literatures. As per the above refinement condition, for the best fitting, the fitting parameters, χ^2 is found to be minimum i.e., 1.33, where GOF=1.20, Rp=22.3% and Rwp=28.6%. It indicates the goodness of fitting. With this fitting, cell parameters and cell volume are found to be a=b=5.7163(1) Å, c=9.2435(4) Å, c/a=1.616 and 302.037 Å^3 for tetragonal phase, and a=b=c= 8.189(2)Å and 549.071 Å^3 for cubic phase. The position coordinates (X, Y, Z) for the oxygen are found to be (0, 0.5200, 0.2432) and (0.2640, 0.2640, 0.2640)

corresponding to tetragonal and cubic phase, respectively. Isotropic displacement (B_{iso}) is found to be 0.81, 1.65 and 1.72 $Å^2$ for A site, B site and oxygen, respectively, for the tetragonal phase. Similarly, B_{iso} for the cubic phase is found to be 4.5, 3.4 and 0.9 $Å^2$ corresponds to A site, B site and oxygen, respectively. The phase fraction for tetragonal phase is estimated to be 91.84% and 8.16% is for cubic phase.

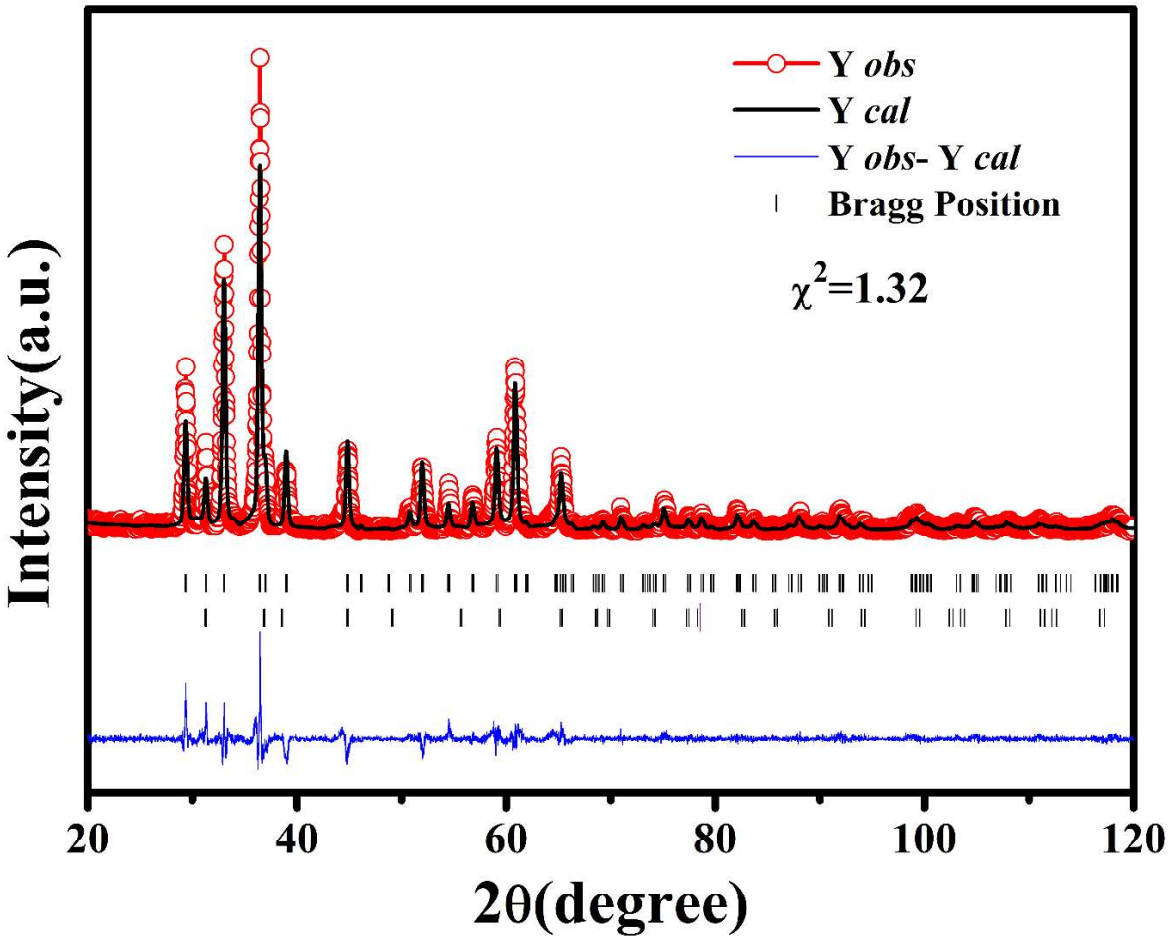

Figure 3.2: Experimental XRD pattern fitted with Rietveld refinement of FullProf program along with the difference pattern between experimental and calculated one of $CoMn_2O_4$ nanoparticles.

Table 3.1: Structural parameters of $CoMn_2O_4$ nanoparticles at room temperature revealed from the Rietveld refinement.

	Tetragonal	**Cubic**
Setting	Origin 2	Origin 2
Space group	$I41/amd$	$Fd\bar{3}m$
a [Å]	5.7163 (1)	8.189 (2)
b [Å]	5.7163 (1)	8.189 (2)
c [Å]	9.2435 (4)	8.189 (2)
Vol [Å^3]	302.037 (2)	549.072 (2)
Co/Mn (A site)	4b (0, 1/4, 3/8)	8a (1/8, 1/8, 1/8)
Biso [Å^2]	0.81 (6)	4.5 (8)
OccA/Co [%]	94	4
OccA/Mn [%]	6	96
Co/Mn [B site]	8c (0, 0, 0)	16d (1/2, 1/2, 1/2)
Biso [Å^2]	1.65 (4)	3.4 (6)
OccB/Co [%]	3	48
OccB/Mn [%]	97	52
O	16h (0, y, z) x: 0 y: 0.520 (1) z: 0.2432 (5)	32e (x, y, z) x: 0.2640 (3) y: 0.2640 (3) z: 0.2640 (3)
Biso [Å^2]	1.72 (12)	0.9 (11)
Phase fraction	91.84 (0.60)	8.16 (0.65)
Bond length	(O-A): 1.966 (0) $(O\text{-}B)_{ax}$: 2.251 (5) $(O\text{-}B)_{eq}$: 1.943 (5)	(O-A): 1.97 (4) $(O\text{-}B)_{ax}$: 1.94 (4) $(O\text{-}B)_{eq}$: 1.94 (4)
Bond angle	O-A-O: 103.4 (4) A-O-B: 125.4 (3) O-B-O: 94.8 (3) B-O-B: 94.7 (3)	O-A-O: 109 (2) A-O-B: 120.5 (1) O-B-O: 97.0 (1) B-O-B: 96.6 (1)
χ^2	1.330	
Rp [%]	22.3	
Rwp [%]	28.6	
GOF	1.2	

Generally, $CoMn_2O_4$ is a normal spinel compound crystallized in tetragonal structure where Mn^{3+} occupy the octahedral site and Co^{2+} occupy the tetrahedral site [83]. However, depending on the annealing temperature and the SiO_2 content in $CoMn_2O_4$ synthesized through a wet chemical method, both cubic and tetragonal phases coexist [114]. The normal spinel which is tetragonal in nature like in Mn_3O_4, the inverse spinel is assigned to the cubic phase like in case of Co_3O_4 [26]. The reported literature shows that if the concentration of Mn^{3+} ions in the octahedral sites remains higher than 55%, the structure leads to normal spinel with tetragonal symmetry. However, for lower Mn^{3+}content in the octahedral sites, it becomes an inverse spinel with cubic symmetry [102]. In the present case, from the Rietveld refinement, the presence of Co^{2+}, Mn^{2+}, Co^{3+} and Mn^{3+} revealed for both cubic and tetragonal phase. Thus, the cation distribution for tetragonal and cubic phase are $(Co_{0.94}Mn_{0.06})[Co_{0.06}Mn_{1.94}]O_4$ and $(Co_{0.04}Mn_{0.96})[Co_{0.96}Mn_{1.04}]O_4$, respectively. Similar cation distribution has shown by Humbe et al., for spinel ferrites [152]. The bond lengths and bond angles are given in **Table 3.1**. It is known in spinel that the angle between A and B through oxygen is near to 180^0, it gives rise to greatest exchange energy and the energy decreases very rapidly with increasing distance between the cations A and B. From **Table 3.1**, it is observed that while A-O distance of both phases are almost similar, the $(O\text{-}B)_{ax}$ and the bond angle A-O-B are higher in case of tetragonal phase compared to the cubic one.

In $CoMn_2O_4$, synthesized by thermal decomposition at temperature 800 ºC and 1000 ºC, the crystallite size increases from 30 to 40 nm with the increase in cell volume from 303.64 and 303.76 $Å^3$, respectively [80]. The octahedral bond lengths such as $(O\text{-}B)_{ax}$ and $(O\text{-}B)_{eq}$ are found to be 2.245 (2) and 1.9781 (3) respectively for the above-reported particles of 40 nm [80]. In order to examine the reason behind the decrease in cell volume in the present case, we have determined the particle size from Williamson-Hall analysis

[153]. The contribution of particle size and strain is estimated by subtracting the contributions of $K\alpha_2$ and instrumental broadening from the FWHM of the various Bragg peaks. Williamson–Hall (W-H) analysis is carried out using equation (3.1) and the particle size, strain are estimated from the plot $\frac{\beta cos\theta}{\lambda}$ versus $\frac{sin\theta}{\lambda}$ where θ is Bragg angle

$$\frac{\beta cos\theta}{\lambda} = \frac{k}{D} + \frac{4\varepsilon sin\theta}{\lambda} \quad (3.1)$$

From the W-H plot, while a straight line parallel to the $\frac{sin\theta}{\lambda}$ axis for pure particle size broadening is expected, the non-zero slope indicates the strain in the lattice. The crystallite size obtained from the intercept is found to be 42 nm and the strain in the lattice is 0.0014. As the crystallite size is comparable to the reported literatures, the effect of size on cell volume is eliminated. Further, the octahedral bond lengths such as $(O\text{-}B)_{ax}$ and $(O\text{-}B)_{eq}$ are reported for samples of size 40 nm as 2.245 (2), 1.9781 (3), respectively. In the present case, we observe that while $(O\text{-}B)_{ax}$ is increased to 2.251 (5), $(O\text{-}B)_{eq}$ is decreased to 1.943 (5). The significant decrease in $(O\text{-}B)_{eq}$ could contribute to the decrease in volume.

The valency of Co and Mn obtained from the Rietveld analysis is further confirmed from X-ray photoelectron spectroscopy (XPS). We have fitted the spectrum by handling XPS software peak 4.1 and have calibrated with carbon-1*s* peak at 284.6 eV. The presence of Co, Mn, O and carbon as reference is shown in the survey spectrum **Figur 3.3(a)**. The spectrum of Co 2*p* shown in **Figure 3.3(b)**, indicates four sharp peaks in which two prominent peaks at 796.077 and 780.67 eV correspond to Co $2p_{1/2}$ and Co $2p_{3/2}$, respectively along with two satellite peaks obtained at 785.5 and 802.3 eV. The binding energy separation between Co $2p_{1/2}$ and Co $2p_{3/2}$ found to be 15.4 eV, confirms the presence of Co^{2+} and Co^{3+} [83,154]. The asymmetric peaks of Co $2p_{1/2}$ and Co $2p_{3/2}$ are further

deconvoluted. While the peaks obtained at 780.3 and 795.6 eV are assigned to Co^{2+}, 782.2 and 797.4 eV correspond to Co^{3+} ions. The estimated intensity ratio of Co^{3+} and Co^{2+} found to be 0.426 gives the concentration of Co^{3+} and Co^{2+} as 29.8% and 70.2%, respectively. Similarly, the spectrum of Mn 2*p* shown in **Figure 3.3(c)**, exhibits two prominent peaks corresponding to Mn $2p_{1/2}$ and Mn $2p_{3/2}$ at 653.4 eV and 641.6 eV, respectively. The asymmetricity observed in both the peaks of Mn 2*p* spectra, has been fitted using four peaks with binding energy of 641.48, 643.64, 652.77, and 654.25 eV. The binding energy separation of deconvoluted peaks situated at 641.48 and 652.77 eV found to be 11.3 eV which confirms the presence of Mn^{3+} cation, the binding energy separation of the peak situated at 643.64 eV and 654.25eV found to be 10.6 eV confirms the presence of Mn^{2+} [83,154]. The intensity ratio between Mn^{2+} and Mn^{3+} is found to be 0.65, which shows the concentration of Mn^{2+} and Mn^{3+} is about 39.39% and 60.60%, respectively. The O 1*s* spectrum shows a peak at binding energy 529.8 eV corresponding to oxygen anion (O^{2-}) present in the sample. O 1*s* spectrum is fitted with three peaks (**Figure 3.3(d)**). Peak situated at binding energy 529.6 eV and 531 eV while indicates the lattice oxygen, peak present at the binding energy 532.9 eV indicates the presence of oxygen defects [83]. The defects are found to be 17%. XPS analysis although confirms the presence of Co^{2+}, Mn^{2+}, Co^{3+} and Mn^{3+} with oxygen vacancies. Further, the presence of Co^{3+} and Mn^{2+} along with major concentration of Co^{2+} and Mn^{3+} corroborates with the presence of cubic and tetragonal phases observed in **Figure 3.2**.

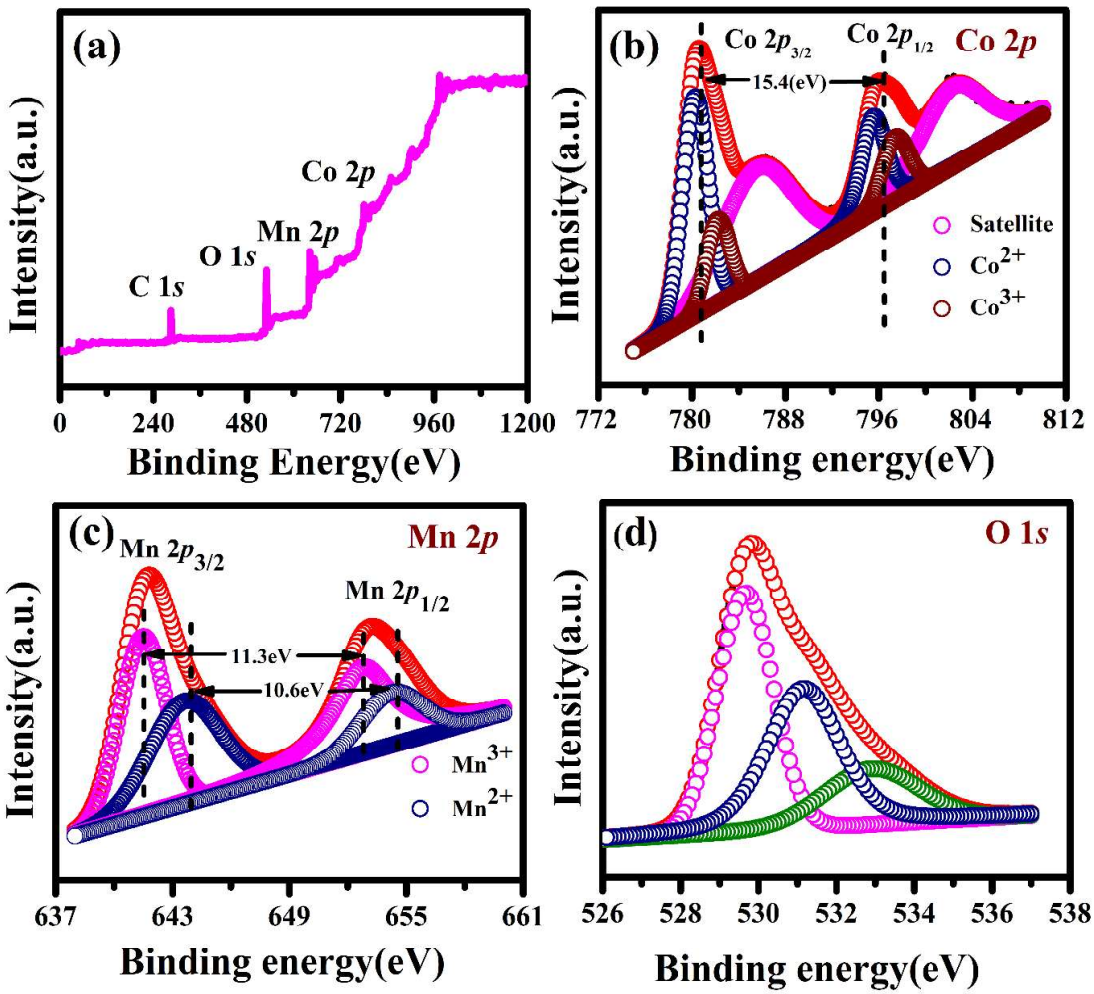

Figure 3.3: X-ray photoelectron spectra of $CoMn_2O_4$ nanoparticles (a) Survey spectrum (b) Co 2p (c) Mn 2p (d) O 1s.

Further structural characteristics have been confirmed via Raman spectroscopic technique at room temperatures as shown in **Figure 3.4**. According to the group theory, the tetragonal $CoMn_2O_4$ with a space group of $I41/amd$ should have ten first-order Raman-modes namely $2A_{1g}$, $3B_{1g}$, B_{2g} and $4E_g$ [131]. Here, we observe six Raman modes present within 100–1300 cm^{-1}. The remaining modes are either too weak in intensity or have energies below the experimental cut-off wave number. The observed broad peaks at 174, 307, 363, 480, 594 and 641 cm^{-1} correspond to B_{1g}, A_{1g}, B_{2g}, E_g, B_{1g} and A_{1g} modes, respectively [131,155]. In the low-frequency region, the first Raman mode B_{1g} is

assigned to the cobalt–oxygen stretching in the tetrahedral site [156]. A_{1g} and B_{2g} modes are related to the oxygen vibrations in both MnO_6 octahedral / MnO_4 tetrahedral site [131,156]. While E_g mode is ascribed to the Co-O / Mn-O movement in tetrahedral site [131,157], high frequency B_{1g} and A_{1g} are assigned to the oxygen vibrations in octahedral site [156].

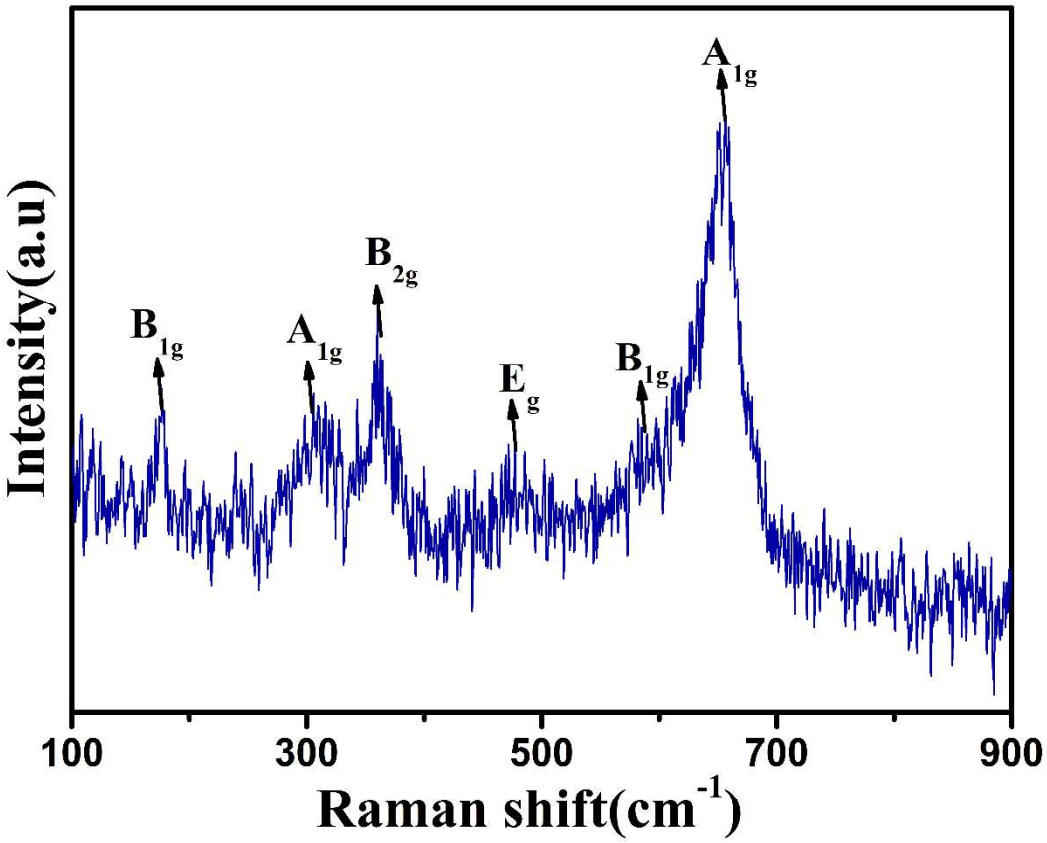

Figure 3.4: Raman spectrum at room temperature of $CoMn_2O_4$ nanoparticles.

3.2.3 Microstructural Analysis through TEM

Transmission electron micrograph depicted in **Figure 3.5(a)**, shows the semi-spherical shape of the particles. The average particle size is found to be 95 nm (approx.) from particle size distribution histogram, as shown in **Figure 3.5(b)**. The interplanar spacing (d) is found to be 0.27 nm corresponding to the (103) plane of tetragonal phase obtained from high resolution transmission electron micrograph **(Figure 3.5(c))**. Diffraction ring patterns observed from the selected area electron diffraction (SAED) pattern, shown in **Figure 3.5(d)**, indicate polycrystalline nature of the particle. The rings are found to be well matched with the (103), (004), (224), (512) and (408) plane of the tetragonal phase. Although, (004) is also matched with the cubic phase of $CoMn_2O_4$.

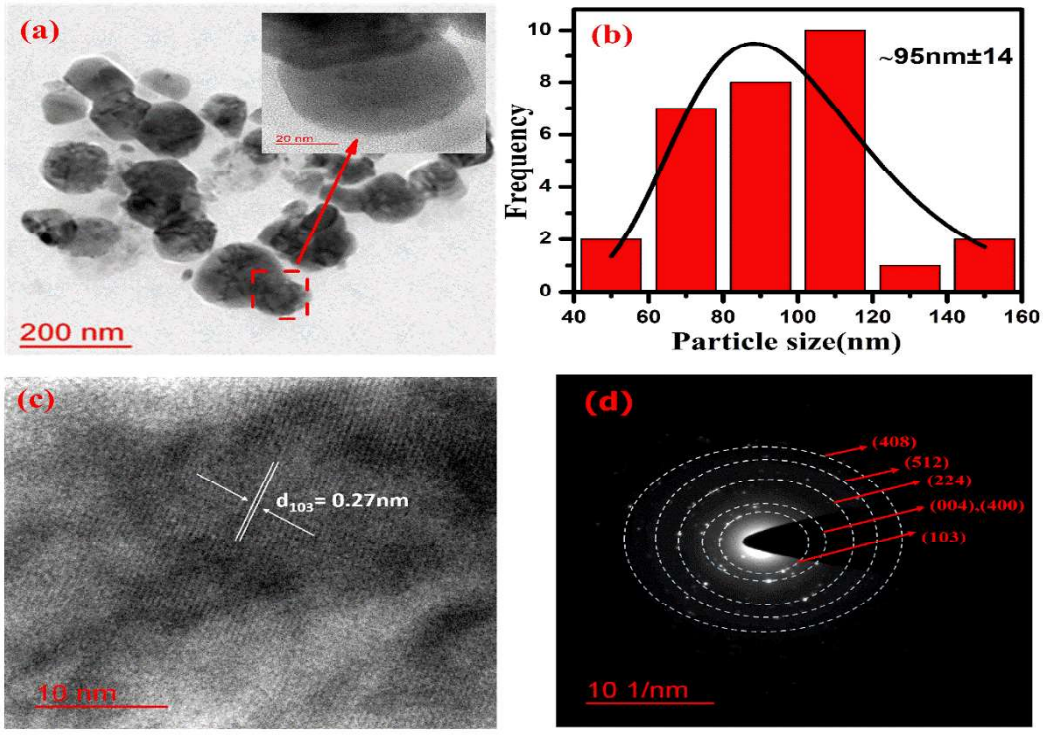

Figure 3.5: (a) TEM, (b) Particle size distribution histogram, (c) HR-TEM image, interplanar spacing, (d) SAED pattern of $CoMn_2O_4$ nanoparticles.

3.3 Magnetic Analysis

3.3.1 Temperature dependent Magnetization

Magnetization (M) of the $CoMn_2O_4$ nanoparticles has been measured with varying temperature and magnetic field (H). The temperature dependent magnetization measured under zero field cooling (ZFC) and field cooling (FC) with an external magnetic field of 0.5 kOe in the temperature range of 3 to 300 K is depicted in **Figure 3.6**. With decrease in temperature, both M_{ZFC} and M_{FC} increase and show a maximum at 136 K (Tp_1). With further lowering the temperature, M_{ZFC} and M_{FC} show another maximum at 87 K known as Tp_2. Two transition temperatures such as Tc_1 and Tc_2 corresponding to the maxima Tp_1 and Tp_2 are thus found out by extrapolation of the linear part of M_{ZFC} to the temperature axis which is shown in the inset of **Figure 3.6(a)**. Tc_1 and Tc_2 are found to be 165 K and 93 K, respectively. These transition temperatures are also confirmed from the inflection in dM/dT vs T curve shown as inset **Figure 3.6(b)**. It is further observed that above Tp_1 the ZFC and FC curves coincide, showing that the system is in equilibrium due to the fast fluctuations of the magnetic moments of the nanoparticles [80]. Thus, below room temperature, while a transition from the paramagnetic to the magnetically ordered state appears at the Tc_1, from low ordered magnetic state, Tc_1 to high ordered magnetic state, Tc_2 is observed. Compared to Tc_1 observed at 165 K in our case, Tc_1 has been reported at 184 K and 190 K [83,122]. In literatures, Tc_1 has been attributed to the presence of some impurity phases related to $Co_{3-x}Mn_xO_4$ [83,122]. However, in the present case, Tc_1 is less compared to literatures and thus eliminates the presence of impurity phase as evidenced from XRD also. Tc_2 is reported at 74 K in case of sol-gel synthesized $CoMn_2O_4$ [83].

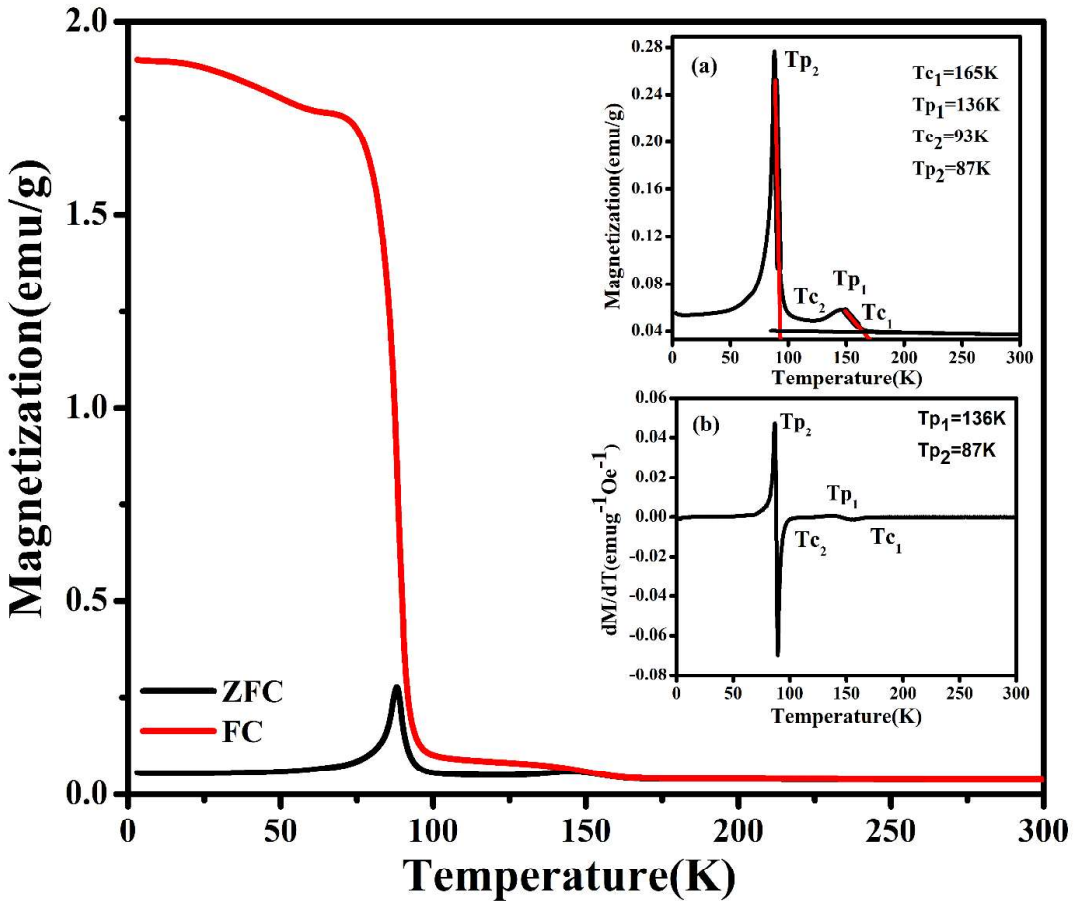

Figure 3.6: FC-ZFC magnetization vs temperature, inset (a) extrapolation of ZFC vs temperature curve and inset (b) dM/dT vs temperature for $CoMn_2O_4$ nanoparticles measured at 0.5 kOe.

Here, one may note that the Tc_1 and Tc_2, could be due to cubic and tetragonal phase of $CoMn_2O_4$ as established from Rietveld analysis. While Tc_1 could be attributed to the cubic phase, Tc_2 represents the tetragonal phase. As reported on cobalt manganite single crystals by Boucher et al., Tc_2 must be due to the presence of Yafet–Kittel spin structures [103]. Mn^{3+} ions present in the octahedral sites give rise to Yafet–Kittel spin structures, Co^{2+}/Mn^{2+} ions occupying the tetrahedral sites show the collinear behaviour in tetrahedral site [80,83] . In the present case, below Tc_2, large concentration of Mn^{3+} cations present in the octahedral sites, attain a non-collinear triangular spin canting

arrangement, and have led to large ferrimagnetic moments. Above Tc_2, there is a vanishing effect of these noncollinear moments among Mn^{3+} ions and thus a reduction in magnetization is evidenced from M–T curve. The cubic phase in which a smaller number of Mn^{3+} cations present in the octahedral site compared to normal spinel configuration of tetragonal phase thus shows reduction in magnetization.

Temperature dependent magnetization at different external magnetic fields is shown in **Figure 3.7**. While the peak observed at Tp_1 and Tp_2 shifts towards lower temperature as expected, the increase in difference between the FC and ZFC magnetization with increase in applied magnetic field at lower temperature is unusual. Generally, with increase in external magnetic field, the difference in ZFC and FC magnetization decreases indicating low anisotropy. However, enhancement in splitting thus indicates an increase in anisotropy with field [49].

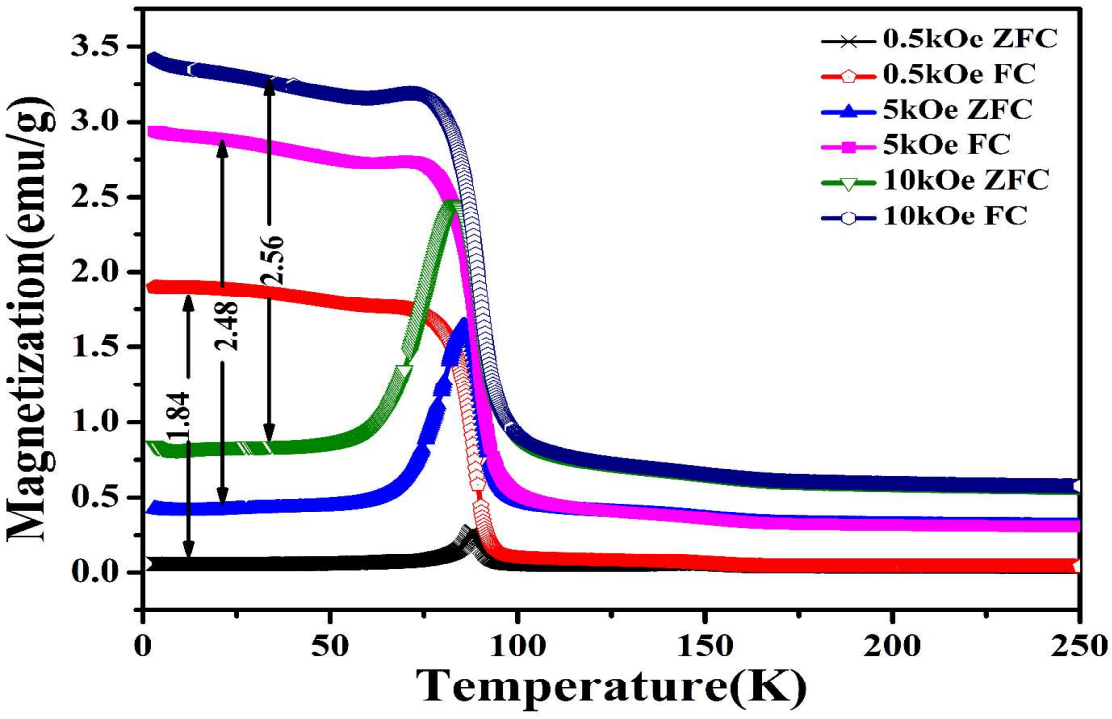

Figure 3.7: Temperature dependent (ZFC, lower branches; FC, upper branches) at 0.5, 5 and 10 kOe.

3.3.2 Field-dependent magnetization

Magnetization versus magnetic field measurement is performed to further understand the magnetic response at different temperatures such as 300 K, 150 K, 120 K, 100 K, 85 K, 50 K, 25 K and 5 K in the magnetic field range of −60 to +60 kOe **(Figure 3.8(a-h))**. Unsaturated hysteresis loop present at higher field for all temperatures, confirms a strong signature of spin canting effect due to antiferromagnetic interactions among the constituent ions in the sub-lattices, presence of an anisotropy and non-linear arrangement of spins. This type of behaviour is normally reported in spinel oxides like Mn_3O_4, $ZnMn_2O_4$, $MgMn_2O_4$ possessing Yafet–Kittel spin structures [158–160]. At room temperature, due to the paramagnetic phase, M-H curve is found to be linear. With decreasing temperature in the vicinity of Tc_1, hysteresis loop area starts to increase. The coercivity, H_C, calculated by $H_C = \frac{|H_C^+|+|H_C^-|}{2}$, where H_C^- is the left coercive field, H_C^+ is the right coercive field of hysteresis loop cutting the $M = 0$ axis taking into account of hysteresis loop gravity centre. It is found to be 0.228 kOe at 150 K which increases to 0.387, 0.542 and 2.375 kOe with decreasing temperature to 120, 100 and 85 K, respectively. Surprisingly, at 50 K, hysteresis loop area significantly increases showing highest H_C of 8.258 kOe. Such high H_C at 50 K, thus an indication of large anisotropy which is evidenced from an increase in splitting of M_{FC} and M_{ZFC} at high field, as shown in **Figure 3. 8(c)**. Further decreasing the temperature to 25 K, while Hc decreases to 3.620 kOe, 0.926 kOe is achieved at 5 K. Such temperature dependent H_C and ZFC magnetization is depicted in **Figure 3.9**. While magnetization shows a maximum at 87 K, H_C is found to be minimum. Hence, temperature dependent H_C and M_{ZFC} behaviour is well corroborated with each other. It is worth mentioning that unlike reported literature on $CoMn_2O_4$ by Kutty et al., where coercivity increases with decrease in temperature [83], we however, observe a coercivity maximum at 50 K followed by a decrease in H_C.

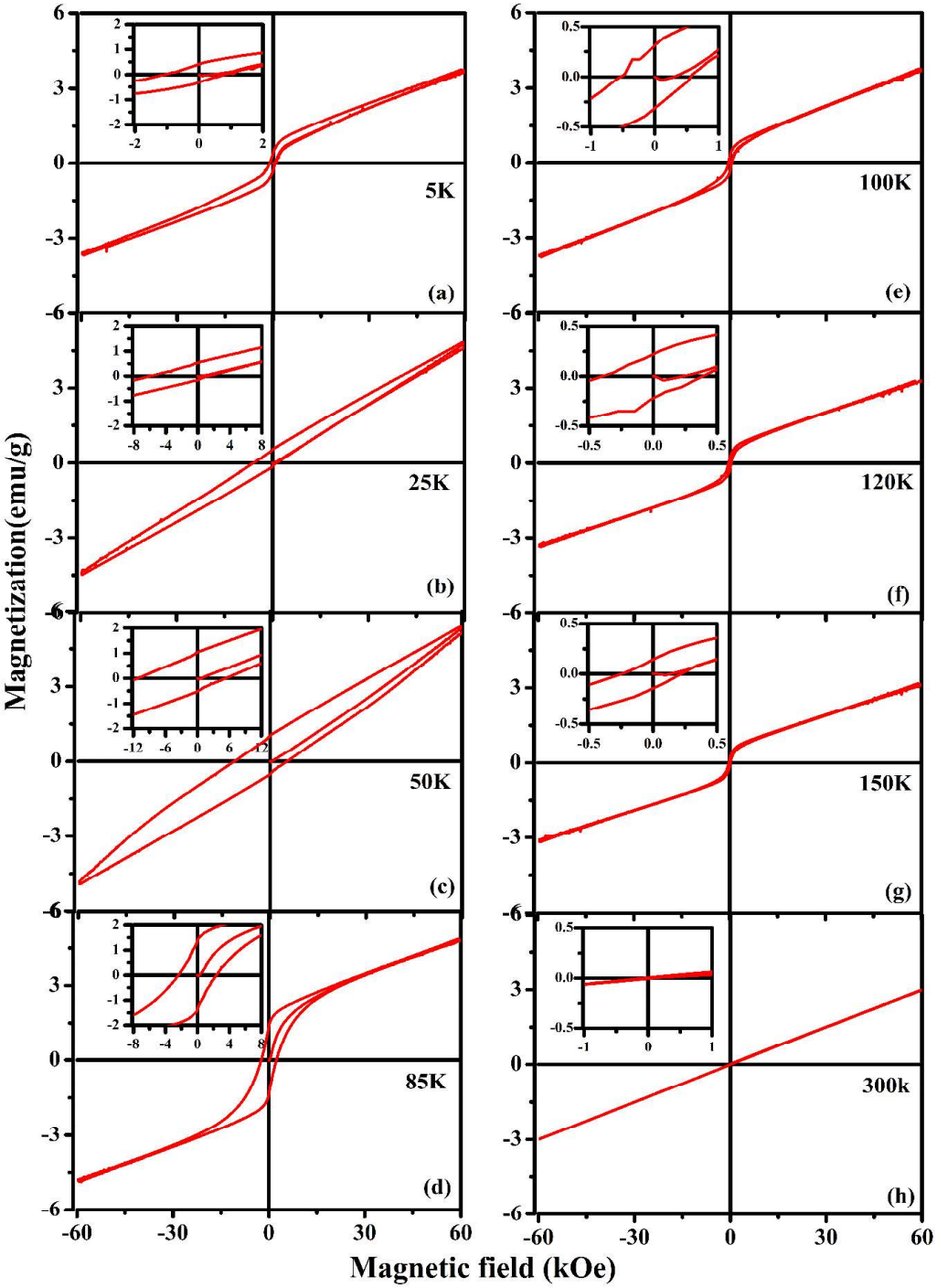

Figure 3.8: Hysteresis loops of $CoMn_2O_4$ nanoparticles at different measuring temperature. Inset indicates the zoomed loop for measuring Hc.

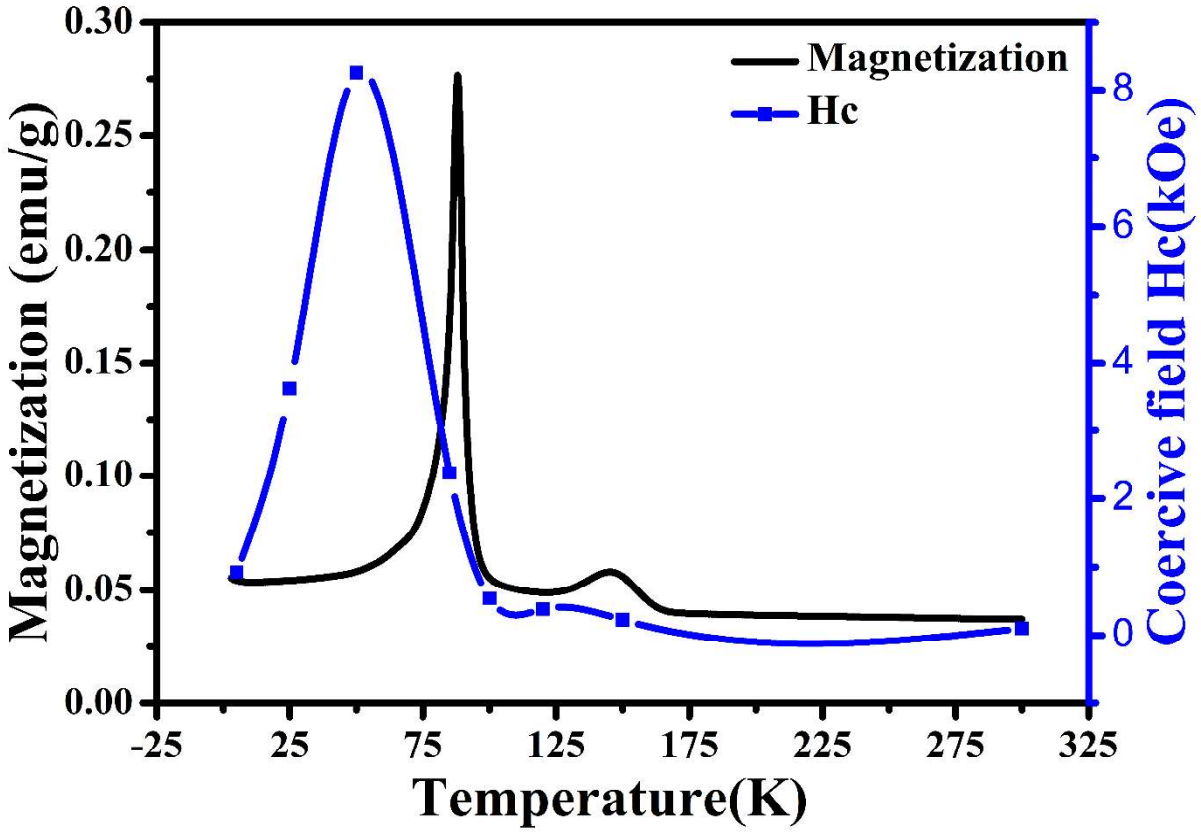

Figure 3.9: Temperature dependent H_C and M_{ZFC} at 0.5 kOe.

3.3.3 Exchange bias and Training effect

The competition between collinear and non-collinear behaviour which develops unidirectional exchange anisotropy and hence, is expected to cause temperature dependent exchange bias field. As evidence, asymmetricity in M-H loops shown in **Figure 3.8**, are observed below 85 K and thus indicates the presence of spontaneous exchange bias (H_{SEB}). The exchange bias field, H_{EB}, is estimated using the relation, $H_{EB} = \frac{|H_C^+ + H_C^-|}{2}$, where H_C^- is left coercive field, H_C^+ is right coercive field of hysteresis loop cutting the $M = 0$ axis. While spontaneous exchange bias, H_{SEB} is absent at 85 K and above, it is found to be 2.971 kOe at 50 K and decreases to 2.325 kOe and 0.137 kOe at 25 K and 5 K, respectively. Further, the conventional exchange bias H_{CEB} from the

hysteresis loop is measured by cooling the sample at 10 kOe from room temperature to the desired temperature. We have carried out the hysteresis loops at 5, 50 and 85 K i.e., below Tc_2. M-H loops under ZFC and FC at 5, 50, 85 K shown in **Figure 3.10(a-c)**. Surprisingly at 5 and 50 K, hysteresis loops shift up in the magnetization (Y) axis. Such kind of shifting is known as vertical magnetization shift (VMS) which has the potential to revolutionize the future of ultrahigh-density magnetic recording technology [59]. It is defined as the shift of gravity centre of the hysteresis loop along the magnetization axis. In literatures, VMS of 0.15 emu/g in $NiFe_2O_4$, 0.2 emu/g in $NiCr_{1.7}Fe_{0.3}O_4$ have been reported. Compared to literatures, we observe one order magnitude higher VMS (2.5 emu/g) at 5 K which decreases to 1.39 emu/g at 50 K and vanishes at 85 K, the vicinity of Tc_2. It is surprising that below Tc_2 i.e., in tetragonal phase with normal spinel, vertical shift is found to be very high. This is because of the Mn^{3+} occupying the B site accompanied with Yafet-Kittel spin structure. While VMS in $NiCr_{1.7}Fe_{0.3}O_4$ is attributed to the impediment of rotation of ferromagnetic moment (FM) moments of A site by the uncompensated antiferromagnetic moment (AFM) moments at B site [161], in $NiFe_2O_4$ it is due to the exchange coupling between the spin-glass like phase and ferrimagnetic phase [61]. The very high exchange bias of 28.587 kOe obtained at 5 K seems to be overestimated due to the non-saturation of magnetization and high irreversibility in magnetization during the hysteresis cycle. To estimate the H_{CEB}, VMS is subtracted from the hysteresis loop to bring back the loop to the centre which is equal to $\frac{|M^{+}_{max}+M^{-}_{max}|}{2}$, where M^{+}_{max} and M^{-}_{max} are magnetization at maximum positive and negative measuring fields [162]. With this correction, H_{CEB} is estimated and found to be 0.635, 3.316 kOe at 5 K and 50 K, respectively. At 85 K, the H_{CEB} is significantly decreased to 0.030 kOe. H_{CEB} is found to be higher than the H_{SEB} at all temperature. While both conventional and spontaneous exchange bias are present below Tp_2, above Tp_2 both are absent.

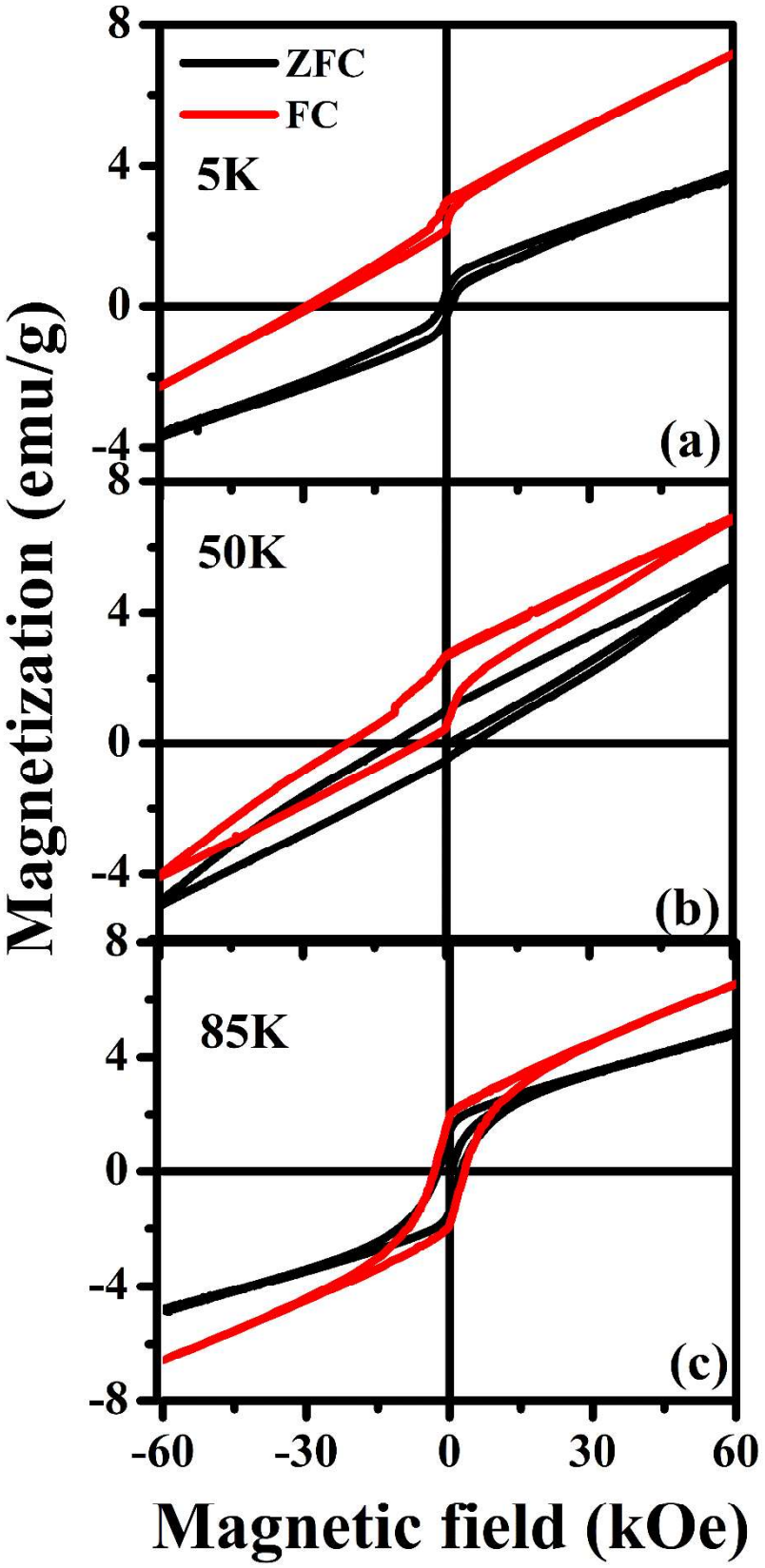

Figure 3.10: FC and ZFC Hysteresis loops measured at (a) 5 K, (b) 50 K and (c) 85 K.

As the exchange bias is maximum at 50 K, we have measured under FC condition at external field of 10 kOe at 50 K and repeated for six cycles. Such measurement is known to be training effect, one of the essential intrinsic characteristics shown due to the presence of the exchange bias in the spinel. H_{CEB} with loop cycle continuously decreases as shown in **Figure 3.11**. Similar kind of behaviour is reported for $NiCr_{1.7}Fe_{0.3}O_4$ normal spinel, where training effect is due to the change in distorted spin configuration with loop cycle [161]. The percentage of training effect (%TE) parameter, which denotes the relative decrease in H_{CEB} starting from the first to last cycle, is estimated using the relation:

$$\%\ \text{of TE} = \left[1 - \frac{H_{CEB}^{1} - H_{CEB}^{n}}{H_{CEB}^{1}}\right] * 100(\%) \qquad (3.2)$$

where H_{CEB}^{1} and H_{CEB}^{n} are the exchange bias fields of first and n^{th} hysteresis loops, respectively [161]. It is observed that %TE abruptly decreases by 82% from the first to second cycle and thereafter, it decreases gradually and tends to saturate with the number of cycles reaching six.

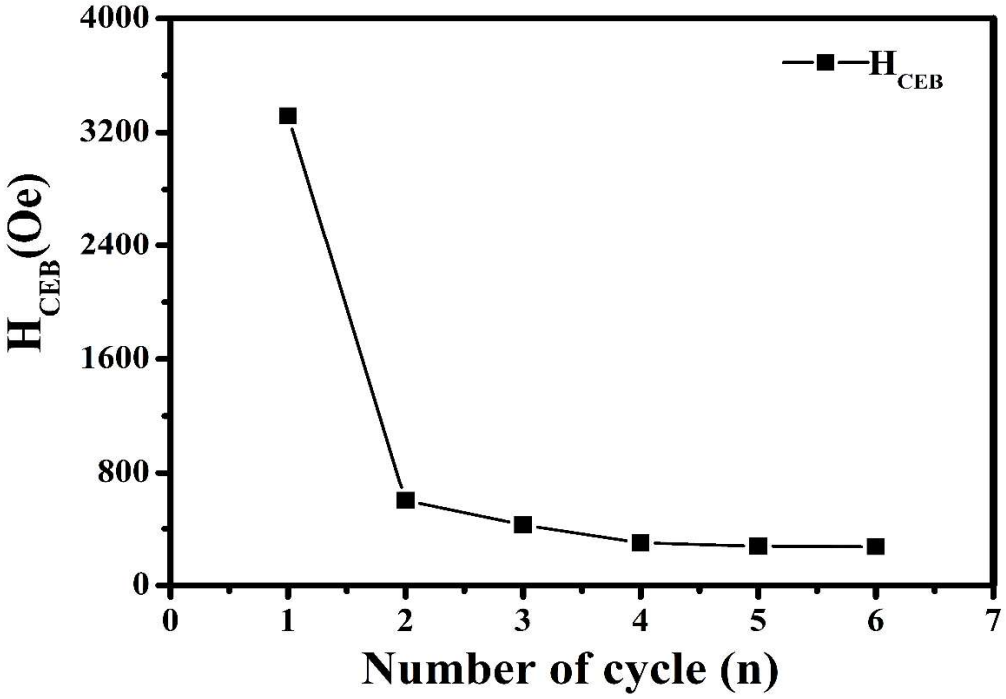

Figure 3.11: Variation of exchange bias with number of hysteresis loop cycles measured at 50 K.

3.4 Discussion

$CoMn_2O_4$ nanoparticles of 42 nm synthesized through co-precipitation route exhibit coexistence of 91.84% of tetragonal phase along with 8.16% of cubic phase. It is further confirmed from Raman spectra and SAED pattern. The predominant presence of tetragonal phase is attributed to the Jahn–Teller distortion due to the 97% of Mn^{3+} cations in the octahedral site. According to the Jahn–Teller distortion, the degeneracy of d-orbital due to the crystal field of the ligand oxygen surrounding Mn^{3+} ions is lifted and the splitting of t_{2g} triplets and e_g doublets distorts the octahedral symmetry, leaves the $d_{x^2-y^2}$ orbitals singly occupied and thus, stabilising the compound in tetragonal symmetry. The extra stability gained in such a way that, it is compensated by the elongation or compression of axial bonds of MnO_6 octahedron, thereby resulting in a distortion. Hence, we observe an elongation along 'a' axis and compression along 'c' axis and c/a ratio found to be 1.616 which is less than the c/a ratio (1.64) observed in Mn_3O_4 [163]. The reduction in c/a ratio could be due to the presence of cubic phase. Further XPS analysis confirms the oxidation states of Co and Mn as +2 and +3 both and higher Mn^{3+} concentration. Two distinct magnetic phase transitions are identified corresponding to paramagnetic to a lower magnetically ordered ferrimagnetic state followed by the higher magnetically ordered ferrimagnetic state at low temperature. While high temperature transition corresponds to cubic phase, latter transition attributes to the tetragonal phase. In ferrimagnetic spinels, sublattice magnetization changes differently with temperature. As evidence, at the time of field cooling, ferromagnetic (FM) ordered spins of tetrahedral A sites easily align in the field direction. In contrast, due to Y-K spin structures, spins at octahedral B sites (mostly Mn^{3+}) do not totally align along the field direction. This is demonstrated by the unsaturated hysteresis loop even up to 60 kOe. As a result of the competition between the spins of tetrahedral and octahedral sites, magnetization

increases, showing maxima at Tp_1 and Tp_2. Furthermore, the asymmetricity in ZFC and FC M-H curves is observed indicating the presence of H_{CEB}, H_{SEB} and VMS. The high exchange bias along with high VMS in $CoMn_2O_4$ is attributed to the combined effect emerging from the competition between collinear (FM) spins and non-collinear spins. These non-collinear spins arise due to Y-K spins of Mn^{3+} cations at octahedral site. Such competition results into a short-range and long-range magnetic ordering below room temperature. Further the presence of exchange bias can be understood as follows; below T_{C2}, when the field is applied and increased isothermally to 60 kOe along the magnetization curve of the hysteresis loop, A site moments and uncompensated moments of B site align along the field direction. When the field is reversed, while FM ordered spins flip along the field direction, spins at B site do not reverse and provide pinning force on the reversible FM spins across the interface. As a result, shift of hysteresis loop along field direction is observed. On the other hand, decrease in VMS with temperature vanishes at 85 K in the vicinity of Tc_2, solely depends on the Y-K spin structure of Mn^{3+} in octahedral site. Aforesaid temperature dependent complex magnetic properties in $CoMn_2O_4$ nanoparticles are ascribed to the mixed spinel configuration with Co and Mn cations of different valences. Furthermore, the exchange bias and VMS phenomenon has important applications in the spin valves, read heads for recording devices, and magnetic tunnel junction-based devices [39,164].

3.5 Conclusion

In summary, we found the structure, microstructure dependence of magnetic properties of $CoMn_2O_4$ spinel nanoparticles. X-ray diffraction pattern fitted with Rietveld refinement, showed the coexistence of 91.84% of the tetragonal phase and 8.16% of the cubic phase at room temperature. The XPS analysis further validated the presence of +2 and +3 oxidation states of Co and Mn. Raman active modes such as B_{1g}, A_{1g}, B_{2g}, E_g, B_{1g}

and A_{1g} confirmed the spinel structure. In agreement with the two structural phases, magnetic transitions at Tc_1 and Tc_2 observed at 165 K and 93 K, corroborated with cubic and tetragonal phases, respectively. An unusual temperature dependent H_C behaviour showed a maximum of 8.258 kOe at 50 K with a high H_{CEB} of 3.316 kOe and H_{SEB} of 2.971 kOe. High VMS of 2.5 emu/g observed at 5 K which decreased with temperature and vanished in vicinity of Tc_2 was discussed on Yafet-Kittel spin structure of Mn^{3+} in B site with collinear configuration of cations in A site. The observations of high exchange bias and VMS hold immense potential for the applications in spin valves, magnetic tunnel junction-based devices and read heads in recording devices.